TUDelft

Delft University of Technology

CT scanning of membrane feed spacers – Impact of spacer model accuracy on hydrodynamic and solute transport modeling in membrane feed channels

Horstmeyer, Nils; Lippert, Thomas; Schön, David; Schlederer, Felizitas; Picioreanu, Cristian; Achterhold, Klaus; Pfeiffer, Franz; Drewes, Jörg E.

Important note
To cite this publication, please use the final published version (if applicable).
Please check the document version above.

CT scanning of membrane feed spacers – Impact of spacer model accuracy on hydrodynamic and solute transport modeling in membrane feed channels

Nils Horstmeyer[a], Thomas Lippert[a], David Schön[a], Felizitas Schlederer[a], Cristian Picioreanu[b], Klaus Achterhold[c], Franz Pfeiffer[c,d], Jörg E. Drewes[a,*]

[a] Chair or Urban Water Systems Engineering, Technical University of Munich, Am Coulombwall 3, 85748 Garching, Germany
[b] Department of Biotechnology, Delft University of Technology, Van der Maasweg 9, 2629 HZ Delft, The Netherlands
[c] Chair of Biomedical Physics, Department of Physics and Munich School of BioEngineering, Technical University of Munich, James-Franck-Str. 1, 85748 Garching, Germany
[d] Department of Diagnostic and Interventional Radiology, Klinikum rechts der Isar, Technical University of Munich, Munich, Germany

ABSTRACT

This study evaluated the impact of precise representation of spacer geometry on numerical simulations of hydrodynamics and solute transport in feed channels of membrane processes. Three levels of increasing geometry accuracy were assessed: i) cylindrical filaments, ii) filaments with circular sections of variable diameter based on microscopic measurements, and iii) geometries obtained from X-ray computed tomography (CT scans) in three resolutions (22 μm, 11 μm, and 5.5 μm). The three-dimensional CT scans revealed quasi-elliptic, not circular, cross-sections of the filaments. Microscopic measurements fail to account for this ellipticity, resulting in over-estimation of pressure drop calculated at industry-typical average velocities (0.07–0.15 m s^{-1}) by a factor of 1.8 compared to CT-based geometries. On the other hand, the cylindrical spacer filaments representation over-estimates concentration polarization at the membrane surface compared to CT-based geometries. Experimental results of pressure drop and particle deposition were in close agreement with simulations using CT scanned geometries. This work demonstrates that modeling results depend significantly on the spacer geometry accuracy. Within the investigated CT scan accuracies 20 μm was found sufficient for modeling hydrodynamics and solute transport in spacer-filled feed channels. The results may be useful for reliable investigation and development of novel spacer geometries.

1. Introduction

Feed spacers are used in spiral-wound membrane modules to create a flow channel between two sheets of adjacent membrane leaves and to potentially enhance feed water mixing so that the build-up of concentration polarization at the membrane surface is attenuated [1]. The most widely applied spacer geometry in practice is the bi-planar net made of extruded polypropylene. It comprises two layers of parallel filaments (non-woven), which commonly form a diamond-shaped layout at a thickness of typically 0.6–0.9 mm (24–36 mil) [2,3]. Spacer filaments deviate from a straight cylindrical shape and exhibit varying thickness ("necking") with the largest diameters at the intersection points [3,4]. Therefore, spacers exhibit a rather complex and irregular geometry.

Spacer geometry is critical to module performance as it directly relates to hydrodynamic and solute transport [5]. The flow field also determines the local distribution of foulants [6]. Thus, for quantitatively reliable fluid flow and solute transport simulations employing computational fluid dynamics (CFD), spacer model geometries close to the original conditions are crucial. However, current spacer geometry modeling is still carried out using far-ranging simplification of the geometry. Two-dimensional (2-D) representations of the cross-flow channel that are used to quickly obtain qualitative results (e.g., by modeling the spacer as an array of circular flow obstacles) were reported to oversimplify the intricate three-dimensional (3-D) hydrodynamics within cross-flow channels [7,8]. Various 3-D CFD studies were conducted to overcome the insufficiency of 2-D models, but were largely limited to simple cylindrical spacer representations [8,9], thus neglecting the variability of the filament diameters. A more accurate representation of spacer geometry was proposed by Picioreanu et al. [7]. In that work, the non-uniform spacer filaments were measured by optical microscopy and the conventionally applied cylindrical strands

---

were replaced by an array of truncated cones with varying diameters. The study revealed that for instance pressure drop computed with the more complex spacer geometry could be twice as high as the one resulting from a simple cylindrical approximation, at flow rates typically applied in engineering practice [7]. This modeling method was further refined, so that the spacers were not only assembled out of truncated cones with edges at the contact boundaries, but also modeled by use of characteristic dimensions and cubic extrusion guides creating smooth filament surfaces [6]. At the same time, measurement techniques also evolved and recently scanning electron microscopy (SEM) was employed to more accurately assess the characteristic dimensions of spacer geometry [4,6].

The latest development in the evolution of spacer geometry accuracy was proposed by Haaksman et al. [10]. In that work, an X-ray computed tomography (CT) scan was carried out to obtain accurate 3-D geometries for any given spacer design. CFD results revealed that the CT scan approach allows for a better quantification of local distribution of velocity and shear [10]. However, a study that simulates solute transport on CT scanned spacer geometries is still lacking, while recent studies aiming on CFD modeling and mass transfer still use the cylindrical geometry [11,12]. Also, a conclusive assessment on how the CT scan accuracy effects hydrodynamics and solute transport simulations in the feed channel is missing. Siddiqui et al. [13] investigated the accuracy of different porosity quantification methods of spacer-filled feed channels and the impact on hydrodynamic predictions. Results showed that the microscopic techniques deviate significantly from the more accurate methods for feed-channel porosity measurements (i.e., volume displacement technique, weight and density technique, CT scanning technique) [13]. Deviations in porosity measurement accuracy can result in a significantly different prediction of the pressure drop of − 31% to 43%, with CT scanning being the recommended porosity measurement technique aimed for numerical studies [13]. However, the accuracy of geometry (and thus, porosity) determination depends heavily on the CT scan resolution. Thus, this study aims (i) to validate the proposed CT scanning approach by modeling hydrodynamics, particle deposition and solute transport within the feed channel, (ii) to verify modeling results of pressure drop and particle deposition through experimental tests, and (iii) to apply the most accurate CT scan up to date to investigate the influence of the CT scan accuracy on CFD and solute transport simulations. In addition, we present here a simplified workflow of converting raw CT scan data to solid shape data to generate the model geometry usable in CFD and solute transport simulations. The development of a periodic computational domain, which is also delineated within this work, allows to reconstruct a spacer net and is applied for numerically efficient particle deposition and solute transport modeling.

2. Materials and methods

2.1. CT scanning procedure

The geometry of a commercially available diamond-shaped spacer (Toray Industries, Inc., Tokyo, Japan) with a thickness of 34 mil (0.86 mm) was assessed by use of computed tomography (CT) scans. The scan of a piece of this spacer comprising 2×3 full rhomboidal mesh elements was executed with a ZEISS Xradia 500 Versa X-ray CT microscope (Carl Zeiss AG, Oberkochen, Germany), using the cone beam of a transmission tube (nt100, Nordson Dage) at a voltage of 60 kVp, power of 4.5 W with a tungsten target and no additional filter. 3601 projections were collected for full (360°) rotation of the sample. The sample was mounted with polystyrene on the sample holder. Fig. 1 displays images of the investigated spacer mesh and the fixed layout of the measurement in the X-ray microscope. The region of interest (ROI) for all measurements was the mesh element nearest the support but still uncovered by the polystyrene (avoidance of potential movement of the spacer during measurement). The data reconstruction was done with the Scout-and-Scan™ Control System Reconstructor (version 11.1.5707) and saved in digital imaging and communications in medicine (DICOM) format as attenuation values. The DICOM data where read into VGStudio MAX (version 2.0, Volume Graphics GmbH, Heidelberg, Germany), converted into isosurfaces by thresholding, and stored as 3-D stereo lithography (STL) file.

The ZEISS Xradia 500 Versa CT microscope uses a two-step magnification of the sample. A geometric magnification of the sample projection onto a scintillator screen is done via the source to object distance (SOD), and the object to scintillator distance (OSD). With the SOD fixed at 70 mm and the OSD at 18 mm, the geometric magnification was $M_{geo} = (SOD + OSD)/SOD = 1.26$ in all experiments. The scintillator converts X-rays into visible light. Switchable magnifying optics between scintillator and detector (iKon-L DW936N BV, Andor) magnifies the scintillator image further. The $4\times$ optical magnification (M_{opt}) of the ZEISS CT microscope was used in the experiment due to the optimal combination of resolution and scintillator efficiency. The detector has 2048×2048 pixels of $13.5 \times 13.5\,\mu m$. Binning into 1024×1024 pixel of $27 \times 27\,\mu m$ (bin2), 512×512 pixel of $54 \times 54\,\mu m$ (bin4) and 256×256 pixel of $108 \times 108\,\mu m$ (bin8) was performed for the three measurements at the three effective, i.e. binned, pixel sizes $r_D = 27$, 54 and 108 μm. The spot size of the X-ray source was determined by the knife-edge method to be $S = 2.2\,\mu m$ at 60 kVp and 4.5 W. Due to the small geometric magnification, this spot size S has only a minor effect on the effective voxel size r_{eff} of the reconstruction (Eq. (1)).

$$r_{eff} = \frac{\sqrt{\left(\frac{r_D}{M_{opt}}\right)^2 + S^2 \cdot (M_{geo} - 1)}}{M_{geo}} \qquad (1)$$

with r_D the binned detector pixel size, S the spot size of the X-ray source, M_{opt} the optical magnification ($M_{opt} = 4$) and M_{geo} the geometric magnification ($M_{geo} = 1.26$). Repeating the tomography with changed detector pixel sizes r_D by binning, the resolution was changed without changing the other parameters of the measurement. The effective voxel size of the reconstructed object was $r_{eff} = 5.44\,\mu m$ (bin2), 10.77 μm (bin4) and 21.50 μm (bin8), referred to in the following as 5.5, 11 and 22 μm CT scan accuracies.

2.2. Surface fitting of the CT scanned feed spacer, solid shape and periodic geometry conversion

The transformed output data format of the CT scanner, a 3-D STL file of the spacer specimen, was not directly usable within the employed CFD software, COMSOL Multiphysics (version 5.3, Comsol Inc., Burlington, MA, USA). Moreover, the STL mesh deviated slightly from the geometric periodicity of the repetitive spacer mesh pattern, possibly due to a slight heterogeneity of the extruded polypropylene fibers resulted during the manufacturing process. However, a periodic geometry is highly desirable for CFD simulations because it allows a significant reduction in the size of a representative computational domain. A solution strategy to overcome these impediments is to precisely remodel the complex geometry, so that a perfectly periodic geometry is created while the utmost of the CT scan accuracy is preserved. This was achieved by use of the Geomagic Design X (3D Systems Inc., Rock Hill, SC, USA) mesh healing and surfacing functionalities, which allow creating solids from a non-uniform polygon mesh. First, the mesh was aligned in an XY-plane and all irrelevant point clouds (due to background noise during CT scanning) lying outside of the spacer geometry were removed via cutting operations. Afterwards the spacer surface was cleared of any holes and defects were repaired (as in [10]), which was done with the further meshing functionalities of Geomagic. To create a precise freeform geometry true to the original scan output, the "Auto Surface Function" of Geomagic was used. This function was able to achieve a high accuracy in the conversion from STL surface triangles
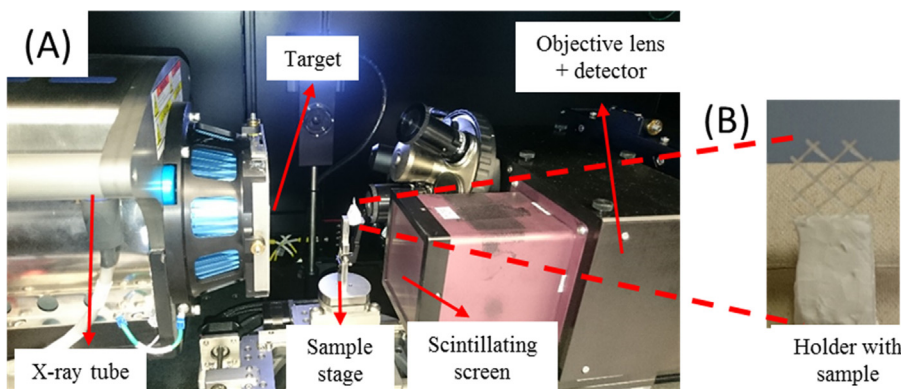
Fig. 1. Microscopic CT scan setup. (A) X-ray microscope with system components: X-ray tube (including electron gun, cathode and electron focus), target, sample stage and detector assembling (including scintillating screen, objective lens and detector). (B) Analyzed feed spacer mesh with 2×3 spacer mesh rhomboids mounted into a polystyrene holder fixed in the X-ray microscope. (C) Schematic of the system components with the two-step magnification of the sample. A geometric magnification (M_{geo}) of the sample projection onto a scintillator screen is done via the X-ray source, the optical magnification (M_{opt}) is achieved by a $4\times$ objective.
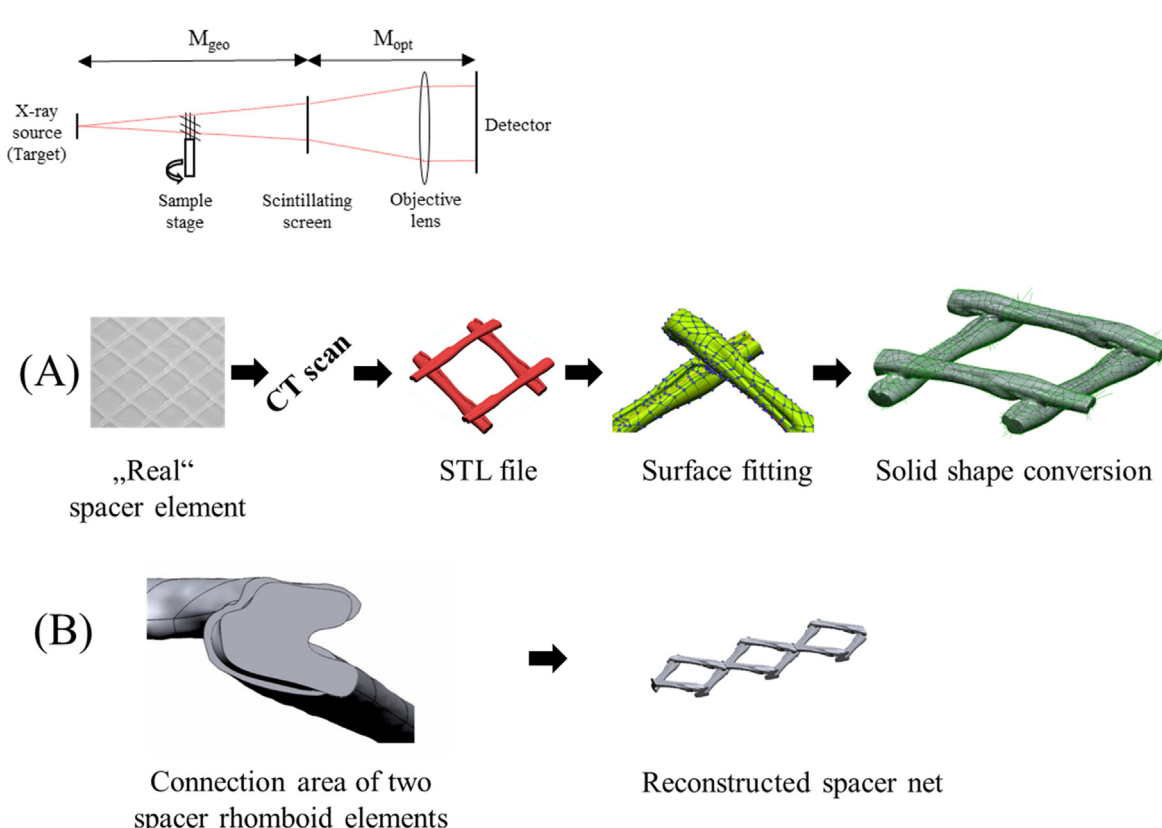

Fig. 2. (A) Workflow of the CT scan approach. The "real" feed spacer was CT scanned, then the STL mesh file was processed for mesh alignment in plane, noise was removed and mesh defects repaired. Subsequently, the repaired geometry was used for surface fitting and conversion into a solid shape. (B) Realization of a periodic feed spacer net. The connection area between two rhomboid spacer elements was matched with a closed spline to create a spacer net.

into a freeform solid by preserving the full detail of the scan (up to 1222 single surface elements in one rhomboid for the 5.44 μm scan accuracy). Subsequently, the geometry was cut on all four intersecting edges. Fig. 2A illustrates the workflow starting with the "real" spacer up to the solid shape conversion for usage in COMSOL Multiphysics.

To impose exact periodicity on the unit geometry the filament openings were matched, i.e. both edges were projected onto one sketch, where a closed spline was created that averages the two original circumferences (Fig. 2B). The closed spline was then used to construct a 0.05 mm thick loft at the edges. This artificial alteration of the CT geometry for the gain of a periodic domain was deemed acceptable, as the difference between the two opening edges was minimal. A spacer mesh was finally created by merging the four lofts with the spacer unit (Fig. 2B). The procedure was subsequently performed for all three CT scan accuracies (22 μm, 11 μm, and 5.5 μm), with results presented in Fig. 3C–E. This new method ensures domain periodicity which allows for an efficient data processing and easy construction of larger spacer nets.

2.3. Derivation of simplified feed spacer geometries

The 3-D CT scan was further displayed in top view in Geomagic Design, corresponding to the conventional microscopic perspective used to measure the spacer dimensions (e.g., in [7,14]). The varying horizontal diameters of each filament were then measured at seven locations on each strand. Based on the measured diameters, circles were drawn and the spacer was rebuilt by extrusion operations, similar to the procedures reported in previous studies [7,10,14]. The resulting two filament segments were vertically placed in a way that the prescribed channel thickness of 0.86 mm (34 mil) was met (Fig. 3B). Finally, the same procedure as in Section 2.2 was applied to create lofts on opposing edges to generate a periodic domain. This simplified spacer geometry is termed here "microscopy-based".

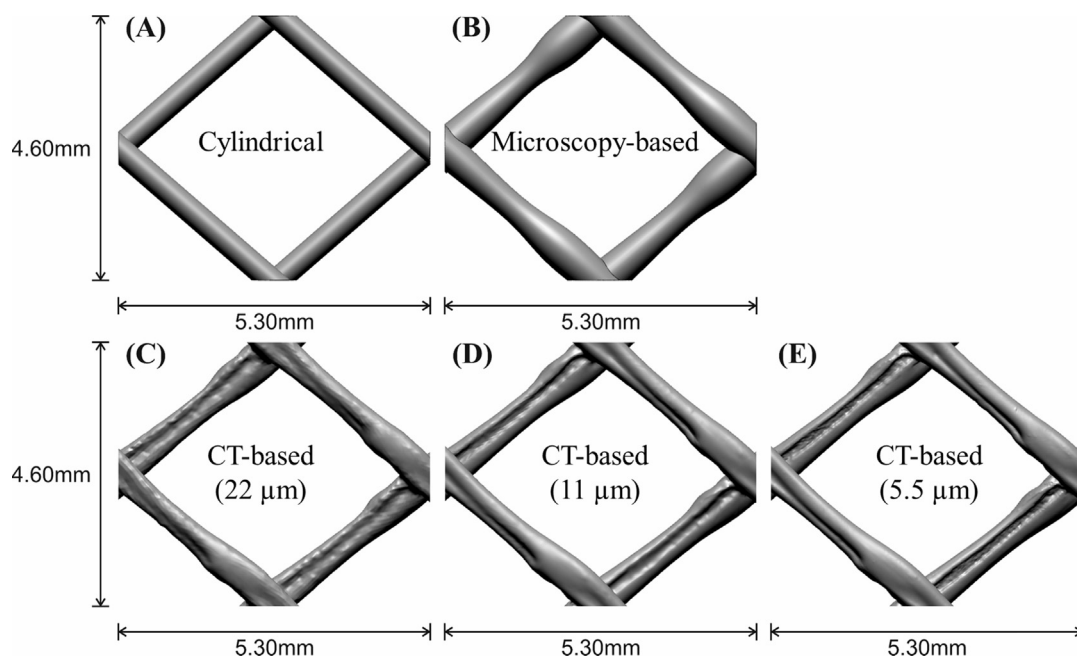The simplified cylindrical spacer representation in Fig. 3A was

Fig. 3. Comparison of the different feed spacer model geometries and CT scan accuracies. (A) Cylindrical filaments; (B) Top-view microscopy-based filaments with circular section; (C–E) remodeled geometries in increasing CT scan accuracy (22 μm, 11 μm, and 5.5 μm). The spacer height is 0.86 mm in all cases.

obtained by replacing the irregular filament geometries by cylinders, with diameters set to half of the channel height (0.43 mm). This is the same procedure used in several earlier 3-D CFD studies [8,9,15–19].

2.4. Fluid domain modeling

The geometries of the fluid domains surrounding the spacers were obtained by subtracting the different spacer geometries (Fig. 3) from blocks with size $4.60 \times 5.30 \times 0.86$ mm. This differential volume corresponds to the water body encasing one spacer mesh element between the lateral faces (periodic in the two lateral directions) and the two membrane surfaces (top and bottom faces). The computational domain for the CT-based spacers is shown in Fig. 4.

2.5. Flow model

Water flow through the spacer-filled feed channel was computed according to the incompressible, laminar, steady-state Navier-Stokes Eqs. (2) and (3):

$$\rho(\mathbf{u}\cdot\nabla)\mathbf{u} + \nabla p = \nabla\cdot(\mu\nabla\mathbf{u}) \tag{2}$$

$$\nabla\cdot\mathbf{u} = 0 \tag{3}$$
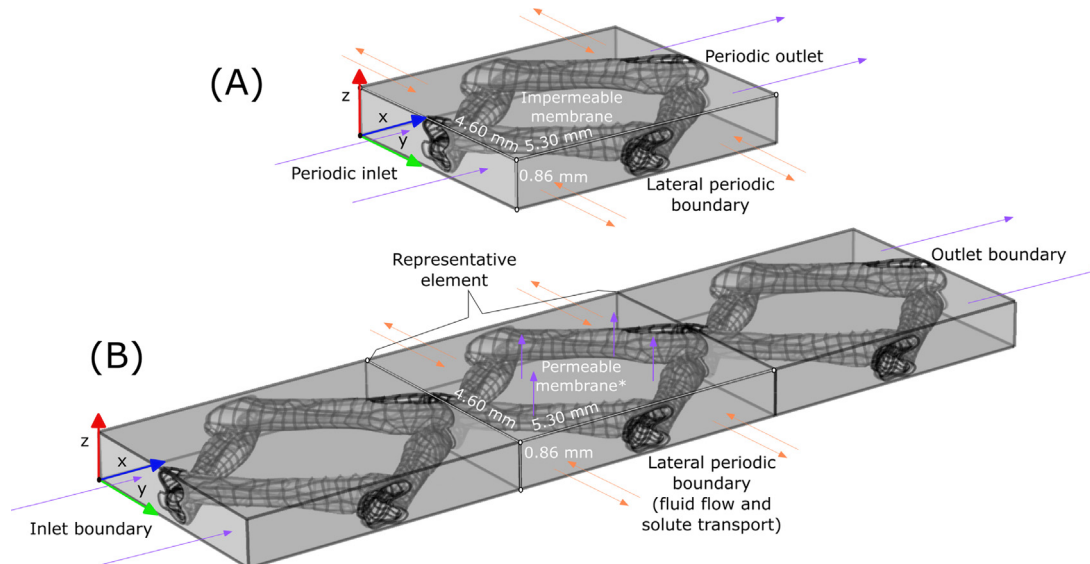
Fig. 4. (A) Periodic domain used for CFD only, with CT-based feed spacer geometries. The flow domain is the difference between a rectangular block and the spacer geometry. The flow with a desired average velocity was driven by a pressure difference set between the periodic inlet and the opposite outlet boundary. No pressure difference was imposed between the lateral periodic boundaries. Top and bottom membrane walls were considered impermeable to flow. (B) Three-element domain used for solute mass transfer calculations. Laminar inflow and ambient pressure outflow were imposed, while the lateral boundaries were periodic. *1 membrane wall was considered permeable for water but impermeable for solutes. Please note that we visualize due to illustration reasons the top membrane permeable in Fig. 4B, while all results show the bottom membrane as permeable membrane.

with $\mathbf{u} = (u_x, u_y, u_z)$ representing the velocity vector, p the pressure, μ and ρ the dynamic viscosity and density of water at 20 °C, respectively. The assumption of laminar flow is justified as solely industry-typical flow velocities ($u_{in} = 0.07$–$0.15\,\mathrm{m\,s^{-1}}$) for the given geometries were tested, corresponding to Reynolds numbers between 84 and 203 (according to Schock and Miquel [20]), in which unsteady or turbulent flow features were shown to be minimal [4,21].

To model fluid flow in a single spacer mesh element and still undisturbed by entrance, exit or lateral wall effects, periodic boundary conditions were set on each pair of parallel lateral faces. The flow was driven by a pressure difference between the periodic inlet and the opposite outlet boundary. An additional constraint (Eq. (4)) iterates this pressure difference until the actual flow rate q_{in} matches the prescribed flow rate $q_{set} = u_{in} \cdot A_{in}$. Hereby, A_{in} is the area of the inlet face (width x height), not accounting for the spacer imprint. Consequently, A_{in} is equal for all tested geometries regardless of spacer accuracy, so that the same q_{set} (and thus q_{in}) is imposed on all different geometries. The total inlet area A_{in} for all domains was equal to 0.86 × 4.60 mm (similar to the approach in [10,6]). Therefore, velocity u_{in} is defined as the average x-component of the flow velocity (normal to the inlet surface) over the total inlet section, with zero velocity taken in the spacer-occupied inlet area.

$$\int_{A_{in}} u_x dA = q_{set} = q_{in} \tag{4}$$

No pressure difference was imposed between the lateral periodic boundaries. For the hydrodynamic simulations, the membrane walls were considered to be impermeable, as the permeation rates typical for nanofiltration (NF) and reverse osmosis (RO) membranes are less than 0.1% of the channel flow rates. This would not affect the flow fields and pressure drop in any significant way (also according to the studies of [6,8,18,22]). Except the periodic boundaries, all surfaces were therefore modeled as no-slip walls. Domain dimensions and boundary conditions are summarized in Fig. 4B and in Table 1.

2.6. Solute transport model

A simplified transport of a model solute through an RO membrane module was also evaluated in this study. When used in conjunction with solute transport, the hydrodynamic model was subjected to several alterations.

First, to calculate 3-D concentration polarization (CP) effects, the membrane boundaries were changed to be permeable for water according to the Darcy model:

$$v_{perm} = \frac{TMP}{R_m \cdot \mu} \tag{5}$$

with v_{perm} representing permeation velocity, TMP transmembrane pressure, R_m hydraulic resistance of the membrane, and μ dynamic viscosity of water (20 °C). As the pressure drop along the computational domain was found to be less than 1/1000 of the operating pressure, a constant permeation velocity of 8 μm/s was chosen based on Eq. (5) for the entire membrane boundary with a TMP of 4.8 bar (70 psi). For R_m, a value of $5.97 \times 10^{13}\,\mathrm{m^{-1}}$ was determined in separate lab measurements for the Toray SUL-G20FTS RO membrane (Toray Industries, Inc., Tokyo, Japan) according to the procedure proposed by Rajabzadeh [23].

Second, membrane permeation caused an unclosed mass balance of water if periodic flow conditions between inlet and outlet were applied. Hence, a laminar flow profile was imposed at the inlet with the prescribed flow rate q_{set}. To avoid strong entrance or exit effects on the solute concentration fields, the domain was extended to a row of three rhomboidal mesh elements and only the middle element was evaluated with respect to hydrodynamics and CP modulus [7]. At the outlet, ambient pressure was set, whereas the lateral boundaries remained unaffected as periodic boundaries.

The transport of solute within the cross-flow channel was modeled by the steady-state convection-diffusion equation, solved using the already calculated flow field $\mathbf{u}$:

$$\nabla \cdot (-D\nabla c) + \mathbf{u} \cdot \nabla c = 0 \tag{6}$$

with D representing the diffusion coefficient (set to $1 \times 10^{-9}\,\mathrm{m^2\,s^{-1}}$) and c the solute concentration. The diffusion coefficient was kept constant, as modeling of a concentration-dependent diffusivity was shown to add considerable computational cost for an only marginal improvement of model accuracy [24]. The membrane was assumed to reject the model solute completely and osmotic effects on permeation velocity were disregarded for this qualitative consideration. With this, the normal component of solute convective flux ($v_{perm} \cdot c_m$) equals the back-diffusion flux ($D \cdot (\partial c/\partial z)_m$) at the membrane surface. These simplifications allow uncoupling the calculation of hydrodynamics from the concentration field. At the inlet, an arbitrary reference concentration of $1\,\mathrm{mol\,m^{-3}}$ was set (since osmotic pressure was not considered), while the outlet boundary was defined as no-diffusion condition. At the lateral boundaries, periodic conditions were applied, and the spacer walls were set as impermeable (no-flux condition).

2.7. Mesh generation

To ensure comparability between the simulation results, all geometries were discretized with the same mesh generation parameters for finite element computations in COMSOL Multiphysics. The domains were meshed by use of a hybrid approach employing both tetrahedron

Table 1
Boundary conditions for the solute transport model.

Boundary surface	Flow model		Solute transport model
	1 – hydrodynamics only	**2 – hydrodynamics with solute transport**	
Inlet	Periodic with outlet	Laminar inflow	Reference Concentration
$x = 0mm$		$u_{in} = 0.07\,\mathrm{m\,s^{-1}}$	$c_{ref} = 1\,\mathrm{mol\,m^{-3}}$
		$u_{in} = 0.11\,\mathrm{m\,s^{-1}}$	
		$u_{in} = 0.15\,\mathrm{m\,s^{-1}}$	
Outlet	Periodic with inlet	Pressure	No diffusion
$x = 15.9mm$		$p = 70\,\mathrm{psi}(4.8\,\mathrm{bar})$	$D_l(\partial c_l/\partial x) = 0$
Lateral boundaries	Periodic condition	Periodic condition	Periodic condition
$y = 0mm$	$u(x, 0, z) = u(x, 4.6, z)$	$u(x, 0, z) = u(x, 4.6, z)$	$c(x,0,z) = c(x,4.6,z)$
$y = 4.6mm$	$p(x, 0, z) = p(x, 4.6, z)$	$p(x, 0, z) = p(x, 4.6, z)$	
Membrane	No-slip condition	Outlet	No flux
$z = 0.86mm$	$u = 0$	$v_{perm} = \Delta p/(R_m \cdot \mu) - v_{corr}$	$D_l(\partial c_l/\partial x) = 0$
Cellholder	No-slip condition	No-slip condition	No flux
$z = 0mm$	$u = 0$	$u = 0$	$D_l(\partial c_l/\partial x) = 0$
Spacer filaments	No-slip condition	No-slip condition	No flux
	$u = 0$	$u = 0$	$D_l(\partial c_l/\partial x) = 0$

Table 2
Key geometric parameters of the different feed spacer models and spacer thickness measurements. The hydraulic diameter calculation was done according to [20].

	Units	CT-based (22 µm)	CT-based (11 µm)	CT-based (5.5 µm)	Microscopy-based geometry	Cylindrical geometry
Porosity	[-]	0.89	0.88	0.88	0.82	0.91
Hydraulic diameter	[mm]	1.05	1.00	1.00	0.91	1.11
Spacer surface area[a]	[mm^2]	23.34	25.20	25.56	27.62	20.22
Spacer thickness (CT scan)[b]	[µm]	810 ± 19	822 ± 7	821 ± 5	–	–
"Canyon" width[c]	[µm]	302	236	195	–	–
"Canyon" depth[c]	[µm]	67	125	100	–	–
Experimental thickness measurements						
Spacer thickness (caliper measurement)[d]	[µm]		848 ± 21		–	–

[a] Per spacer rhomboid element.
[b] Measurements based on 4 measurements at each of the 4 crossings (total 16 measurements).
[c] Measurements based on the broadest and deepest point of the "canyon"-like slot.
[d] Measurements based on 25 caliper measurements distributed over the spacer net.

cells for the bulk volume and hexahedron cells for surface mesh refinements (SMRs). The heavily boundary-influenced fluid flow and solute transport required such SMR to sufficiently resolve the steep velocity and concentration gradients in the wall vicinity at a reasonable number of mesh elements. Bulk volume of the fluid domain was discretized by use of tetrahedron cells, with a maximum and minimum cell size of 138 and 41 µm, respectively, for both fluid flow and mass transport simulations. The tetrahedron mesh was subsequently complemented by adding several layers of an additional hexahedron mesh on the surface boundaries. Decreasing tetrahedron cell size with no usage of such surface mesh refinements proved to be highly inefficient with respect to grid convergence (Supplementary material, Fig. S1). Final meshes featured 8 layers of hexahedron elements for fluid flow and 12 layers of hexahedron elements at the membrane boundary for the mass transport simulation. For fluid flow and solute transport simulations, average total cell counts amounted to 0.65 and 1.15 million elements, respectively. A further increase in cell numbers (by size reduction of the tetrahedron elements or by increasing the number of SMRs) did not lead a notable change in the results. For instance, decreasing tetrahedron cell size by 10% or adding another layer of SMRs (total 9 SMRs) changed the results for pressure drop and average membrane CP modulus by less than 1%.

2.8. Model solution

The stationary laminar flow simulations were carried out in COMSOL Multiphysics 5.3, by using the fully coupled nonlinear solver with PARDISO as the linear solver. Solute transport was subsequently solved based on the previously determined flow field. The simulations were carried out on a workstation with eight Intel(R) Xeon(R) central processing units (CPUs) with 3.16 GHz (GHz) each and 32 GB total random access memory (RAM). The computing time varied between 5 and 48 h per simulation of flow field and between 72 and 96 h per simulation of mass transfer. Simulations were terminated after the residual error between iterations was less than 10^{-3}.

2.9. Particle transport and deposition modeling

Particle transport in the feed channel and deposition on the membrane surface was simulated with a 3-D numerical model, according to [6]. The flow field resulted from COMSOL Multiphysics simulations was exported on a 3-D Cartesian grid for particle distribution calculations in MATLAB (MATLAB R2017a, MathWorks, Natick, MA, USA). The model was applied in three steps: (i) geometric construction, (ii) calculation of fluid flow field around a spacer element, and (iii) particle transport along the fluid streamlines. The movement of particles was computed by a Lagrangian approach, with massless particles following the fluid streamlines. The particles were defined to deposit on the membrane when (i) a particle crossed a threshold distance (5 µm) to the membrane

or (ii) when its velocity was approaching zero. The already deposited particles were considered not to influence the next depositing particles. Particle deposition was simulated with the membrane surface on top of the spacer. More information about this approach can be found in [6].

2.10. Experimental tests of pressure drop and particle distribution and deposition

2.10.1. Pressure drop

The spacer was placed in a flowcell (200 × 40 × 0.86 mm) with a flat-sheet membrane (Toray SUL-G20FTS RO membrane), but without permeation [10,25–27]. The spacer had the same orientation in respect to the flow direction as the model spacer mesh. The flow was controlled precisely with a mass flow controller (Flow X3, Italy). During pressure drop measurements the inflow velocity was increased stepwise (0.07–0.15 m s^{-1}) until steady values were reached. Pressure drop was converted into mbar per 20 cm spacer-filled feed channel. Conversion in Pa/spacer element was determined with 38.5 meshes/20 cm (5.2 mm per mesh). The average inflow velocity (m s^{-1}) was calculated by conversion of the mass controlled flow rate (kg h^{-1}) to volumetric flow rate (m^3 s^{-1}), then divided by the cross-section area (40 × 0.86 mm = 34.4 mm^2), corrected with the porosity (see Table 2). Measurements were replicated three times.

2.10.2. Particle deposition

Particle deposition was followed experimentally in flat-sheet membrane experiments with cross-flow operation and no permeation, as Radu et al. [6] reported the same particle deposition patterns regardless of permeation or no permeation operation. The particle deposition tests were performed with a flowcell of a 146 × 96 × 1 mm, using 34 mil Toray spacer (0.86 mm) and Toray SUL-G20FTS RO membrane. Feed channel height of 0.86 mm was ensured by an acrylic glass of 0.14 mm thickness between flowcell bottom and spacer. A particle feed suspension with red colored latex particle beads (Polybead, Polysciences Inc., Warrington, PA, USA), diameter 2.74 µm, containing approximately 5.6 × 10^8 particles L^{-1} was used for the test in full recycle mode. The duration of the experiment was 6 h. Cross-flow velocity (CFV) was set to (i) 0.35 L min^{-1}, and (ii) 0.74 L min^{-1} (0.07 m s^{-1} and 0.15 m s^{-1} with a cross-section area of 82.6 mm^2 (89 × 0.86 mm)) and controlled by a flowmeter (Blue White Industries, Huntington Beach, CA, USA). Membrane and spacer were analyzed visually directly after the test within the flowcell and with an optical microscope.

3. Results and discussion

3.1. Geometric feed spacer characteristic accuracy
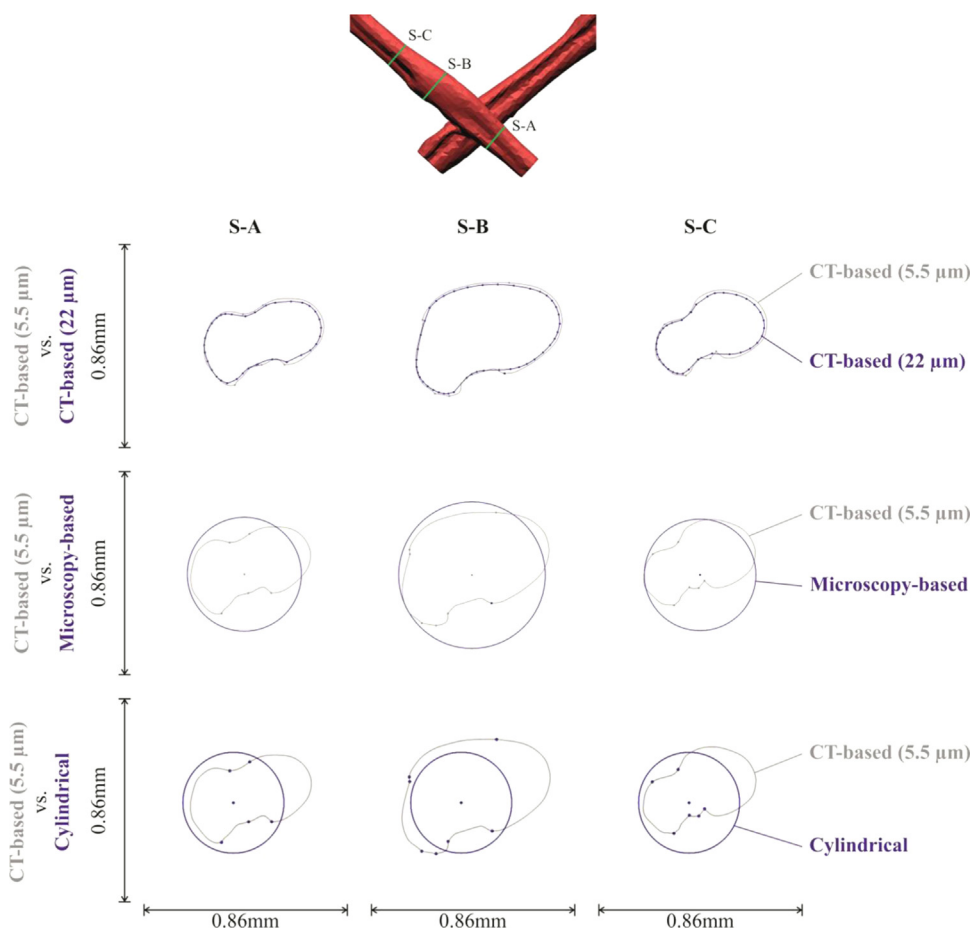
The CT scans of the spacer allowed for an accurate 3-D

Fig. 5. Comparison of cross-sections of the lowest and highest CT-based feed spacer model (22 µm, 5.5 µm) among each other and with the microscopy-based and cylindrical feed spacer model. Each row compares two cross-sections with a black and blue curve, labeled in the left column (For interpretation of the references to color in this figure legend, the reader is referred to the web version of this article.).

measurement of its geometry. CT scans revealed that filament cross-sections strongly deviate from the previously assumed rotationally symmetric shape (Fig. 5). The horizontal diameters (i.e., along the main flow direction) of the irregular sections were found to be considerably larger than the vertical diameters (i.e., along the channel height) for the examined spacer (34 mil, Toray). The cross-sections of the CT-based geometries, depicted in Fig. 5 for the 22 µm and 5.5 µm CT scan accuracy, visualize the quasi-ellipticity of the spacer strands. These findings are in agreement with [10] and confirm the need of the CT scanning approach for numerical simulations. The applied surface fitting method seems to be an appropriate method to i) preserve the accuracy of the CT scan, while ii) enabling efficient CFD simulations by use of periodic domains.

Based on the CT scans, conventional spacer microscopy view from the top was mimicked. No compelling compliance between the two geometry types could be achieved (Fig. 5). While section width and position of the upper domain limit both agree well for raw CT geometries and microscopy-based spacer, filament height (i.e. vertical diameter) is strongly overestimated. As microscopes are only capable of assessing the horizontal diameter accurately, the vertical diameter is inevitably overestimated in a rotationally symmetric spacer model. The prescribed channel height of 0.86 mm dictates a shift of the overly thick filaments towards the middle of the channel in order to fit the microscopy-based spacer model within. As expected, the simple cylindrical model did not achieve a high compliance with the CT-based geometries either (Fig. 5). The deviation between the cross-sections of cylindrical model and CT scan geometry is not as pronounced as for the microscopy-based model with respect to height overrating and vertical offset. The microscopy-based model deviates clearly from the CT-based geometries as porosity and hydraulic diameter were considerably smaller, whereas filament surface was larger (Table 2). The cylindrical model

shows reversed deviations as the surface area is much smaller and the hydraulic diameter is larger.

In contrast to the simplified geometries, the three CT-based geometries (22 µm, 11 µm, 5.5 µm) do not exhibit significant deviations, as presented in the Supplementary material (Fig. S2 and S3). Flow channel porosity and hydraulic diameter were identical for the 11 µm and 5.5 µm CT scan geometry, whereas the spacer surface area, spacer thickness and "canyon" width and depth were in close agreement. The "canyon"-like slots in the filaments were more precisely reproduced at the high CT scan accuracies (as visualized in Fig. 3 and listed in Table 2). The more precise reproduction of the "canyon"-like slots in the spacer strands could be important if (bio)fouling aspects are considered, since these recesses provide a suitable place for the attachment of particles and bacteria. Additionally, the spacer surface appeared rougher with increasing CT scan accuracy. Overall, a lower scan accuracy can lead to a reduced spacer surface area and more imprecise reproduction of the "canyon"-like slots.

Coincidentally, the CT-based and cylindrical models yielded similar values for porosity but geometric compliance is not evident. In comparison with reference caliper measurements, the 11 µm and 5.5 µm CT scans presented the smallest deviations (Table 2). However, the impact of the identified differences and more imprecise reproduction of the 22 µm CT scan accuracy on hydraulic parameters (i.e., pressure drop, velocity profile and shear rate distribution) and solute transport needed to be investigated in detail.

3.2. Impact of feed spacer geometry and CT scan accuracy on hydrodynamics

3.2.1. Pressure drop

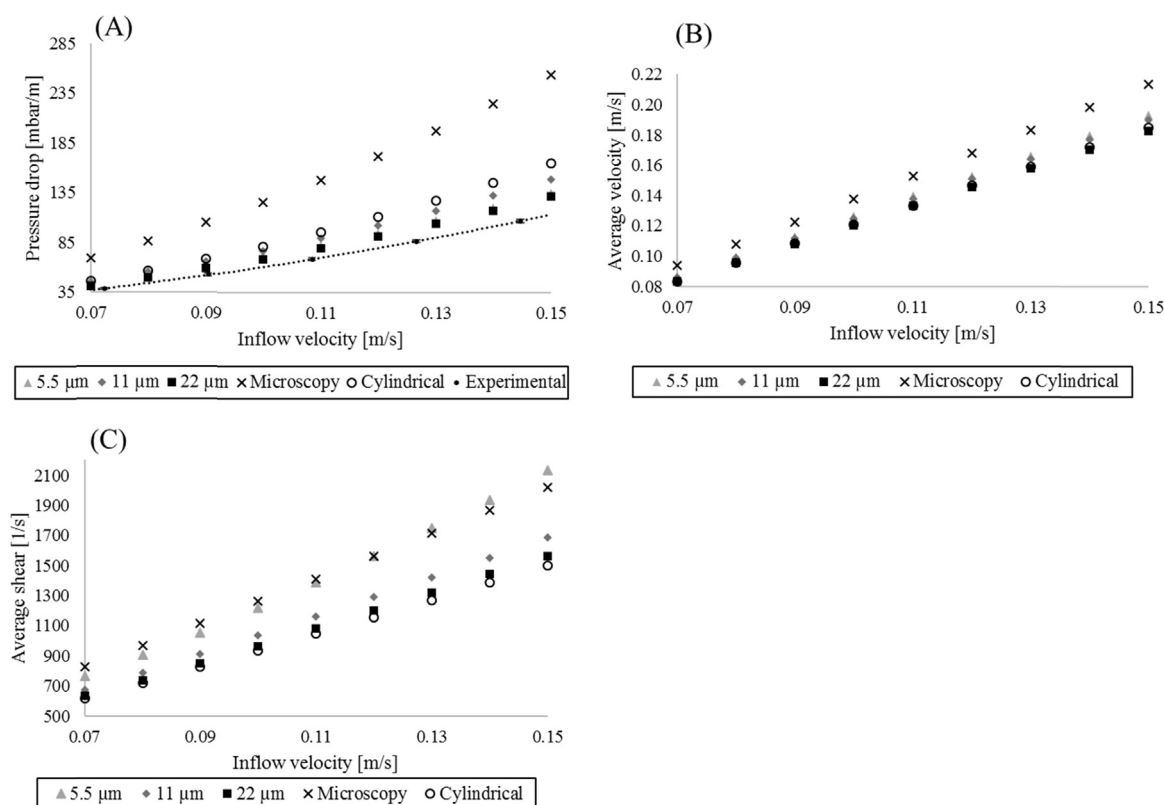The pressure drop over the one-element computational domain was

Fig. 6. Computed dependencies of three hydrodynamic quantities on the average inflow velocities, u_{in}. (A) Pressure drop per meter. Including the comparison of experimental measured mean pressure drop (error bars are shown and represent the standard deviation between determinations with n = 3) and simulated pressure drop. A more detailed representation of the experimental measured data is shown in the Supplementary material (Fig. S4). (B) Volume-averaged velocity. (C) Average shear rate on the membrane.

evaluated for nine inflow velocities ranging from 0.07 to 0.15 m s^{-1} corresponding to a laminar Reynolds number range of 84–203 (Fig. 6A). Pressure drop computed with the microscopy-based geometry was approximately 1.8 times higher than the pressure drop from the CT-based spacer models (22 µm: 1.86 times; 11 µm: 1.65 times; 5.5 µm: 1.77 times). The significant increase in pressure loss for the microscopy-based spacer geometry is due to two factors: i) the reduced channel porosity, which leads to higher average flow velocities and ii) the increased surface area, which results in more friction. Cylindrical and CT-based spacer geometries caused very similar pressure drop ($\Delta p_{Cylindrical}/\Delta p_{CT\text{-}based}$ = 1.20 (22 µm); 1.07 (11 µm); 1.15 (5.5 µm)). However, this effect needs to be interpreted with caution because the similarity stems (most probably) from a coincidentally almost equal porosity and not from a well-matching geometry (Table 2). Finally, the difference between the mean pressure drop (over the whole velocity range from 0.07 to 0.15 m s^{-1}) computed with the most and least accurate CT scan accuracy was less than 5%.

A comparison between experimental measurements of pressure drop function of flow velocity and simulated pressure drop results for the different CT scan accuracies is presented in Fig. 6A. As expected, the measured pressure drop increased quadratically with an increase in velocity, following Bernoulli's law. The experimental measured data were reproducible and in closest agreement with simulations with CT scan geometries with accuracies of 5.5 µm and 22 µm. However, the pressure drop simulations for the CT-based geometries provided higher values than the experimental measurements (in average, 6% at 0.07 m s^{-1} and 14% at 0.15 m s^{-1}). Haaksman et al. [10] also reported a difference of − 7–17% between simulated and measured pressure drop for several different spacer types. The discrepancy could be explained by at least three reasons. First, there could have been a mismatch between the CT scanned geometries and the existent geometry in

the flowcell, resulting from different channel height. Parts of the CT scanned spacer geometry had to be cut off in constructing the modeling domain in order to fit a too thick spacer into the measured channel height, while in experiments the spacer would simply be squeezed [10]. Second, fluid inertia and potential jet effects at the inlet of the flowcell [28] could result in higher pressure drops at higher flow velocities compared to numerical simulations. Thirdly, deviations in slope between experimental and model results at higher flow velocities suggest the transition from steady to unsteady flow, which would invalidate the assumption of steady laminar flow for these velocities. Santos et al. [29] investigated the transition of steady to unsteady flow for 100 < Re < 300, Shakaib et al. [30] reported an onset of unsteady flow for Reynolds numbers between 150 < Re < 175, Haaksman et al. [10] stated an onset of unsteady flow condition for Reynold numbers above 175. Bucs et al. [4] measured a deviation of 10% for Re = 160 between the mean pressure drop from numerical simulations and applied particle image velocimetry measurements. However, direct comparison with other studies is impeded due to the utilization of different spacer model accuracies.

3.2.2. Velocity and shear rate

The observed differences for pressure drop are mirrored in the results for average velocity magnitude (over the whole channel volume) and average shear rates at the membrane (over both top and bottom walls). For the CT-based and cylindrical geometries, both hydrodynamic quantities are similar. However, in the microscopy-based channel geometry the average velocity is ~ 12% higher (22 µm: 9%; 11 µm: 11%; 5.5 µm: 15%) due to the lower porosity (Fig. 6B) and average shear rates are also higher (11 µm: 18%; 22 µm: 28%) compared to the CT-based spacer geometry (Fig. 6C), except for the highest scan accuracy (5.5 µm: ± 5%).
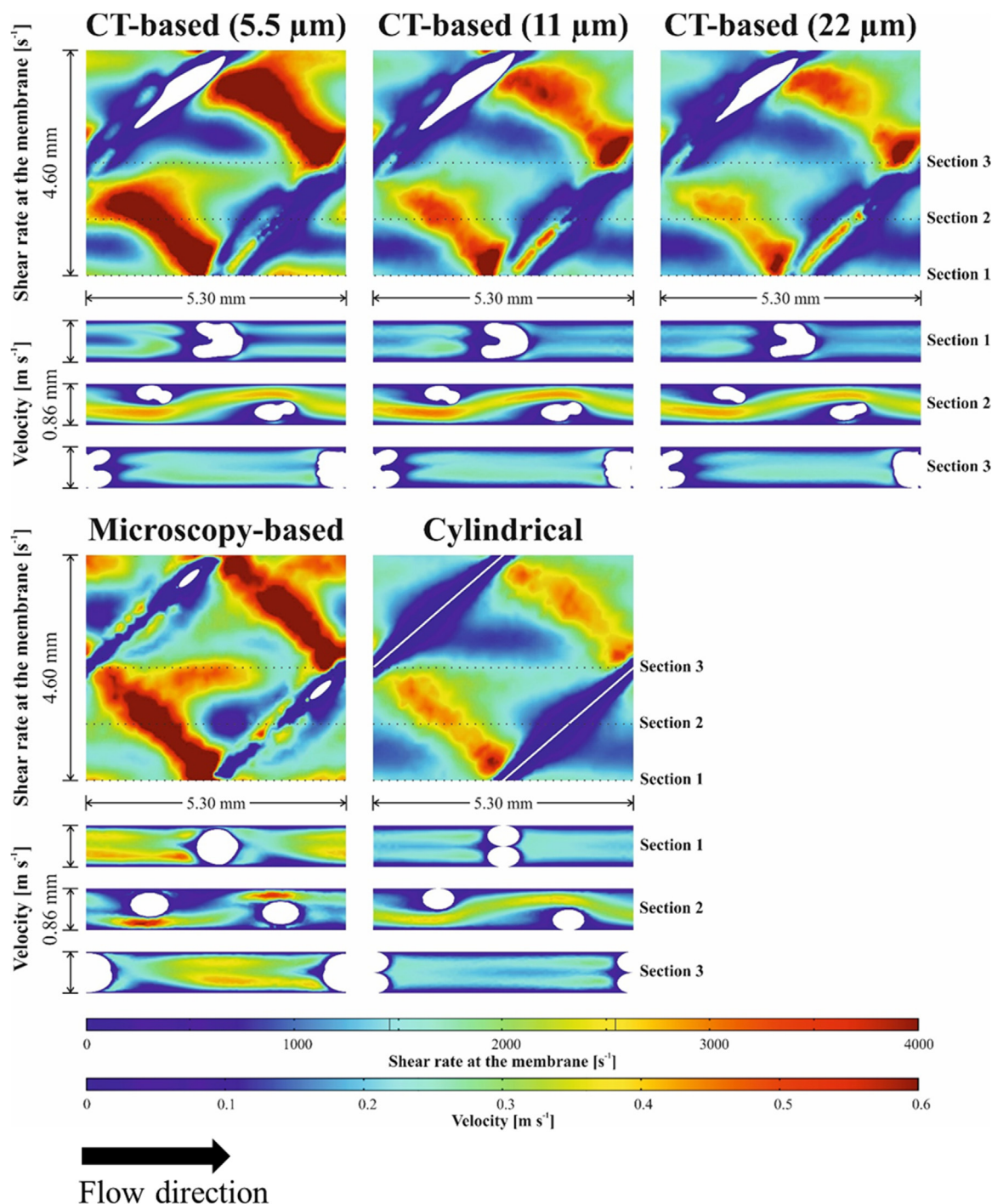
Fig. 7. Comparison of the velocity profiles (bottom panels) and corresponding shear rate distributions at the membrane surface (top panels) for the different levels of feed spacer geometry accuracy, at $u_{in} = 0.15\,\mathrm{m\,s^{-1}}$. The bottom membrane wall is displayed. The high end of the color scale for shear rate was limited to $4000\,\mathrm{s^{-1}}$ in order to make the comparison more visible, whereas the highest shear rate value for the microscopy-based calculations reached about $15,000\,\mathrm{s^{-1}}$.

For all geometries, the shear rate on the membrane presented a largely heterogeneous pattern, with the highest values corresponding the narrow flow sections formed between filaments and membrane. Fig. 7 depicts section plots of velocity profiles and the resulting shear rate distributions on the membrane for a selected velocity of $0.15\,\mathrm{m\,s^{-1}}$. For CT- and microscopy-based geometries, smaller regions of high shear can also be identified along the filament thinnings (neckings), which allow some flow through the narrow gap between membrane and spacer filament. Cylindrical geometries on the other hand - entirely disregarding filament thinning - cannot represent the beneficial effect of filament necking on the shear rate, thus falsely

predicting stagnant water zones (i.e., low shear rate) where spacer filaments touch the membranes.

3.3. Impact of spacer model accuracy on solute transport

The concentration polarization (CP) modulus at the membrane was defined as the ratio between actual concentration and reference concentration of $1\,\mathrm{mol\,m^{-3}}$ in the bulk liquid. High CP values indicate permeate flux reduction due to osmotic effects caused by accumulation of salt next to the membrane in regions with slow mass transfer. The calculated average CP modulus on whole membrane surface, for the
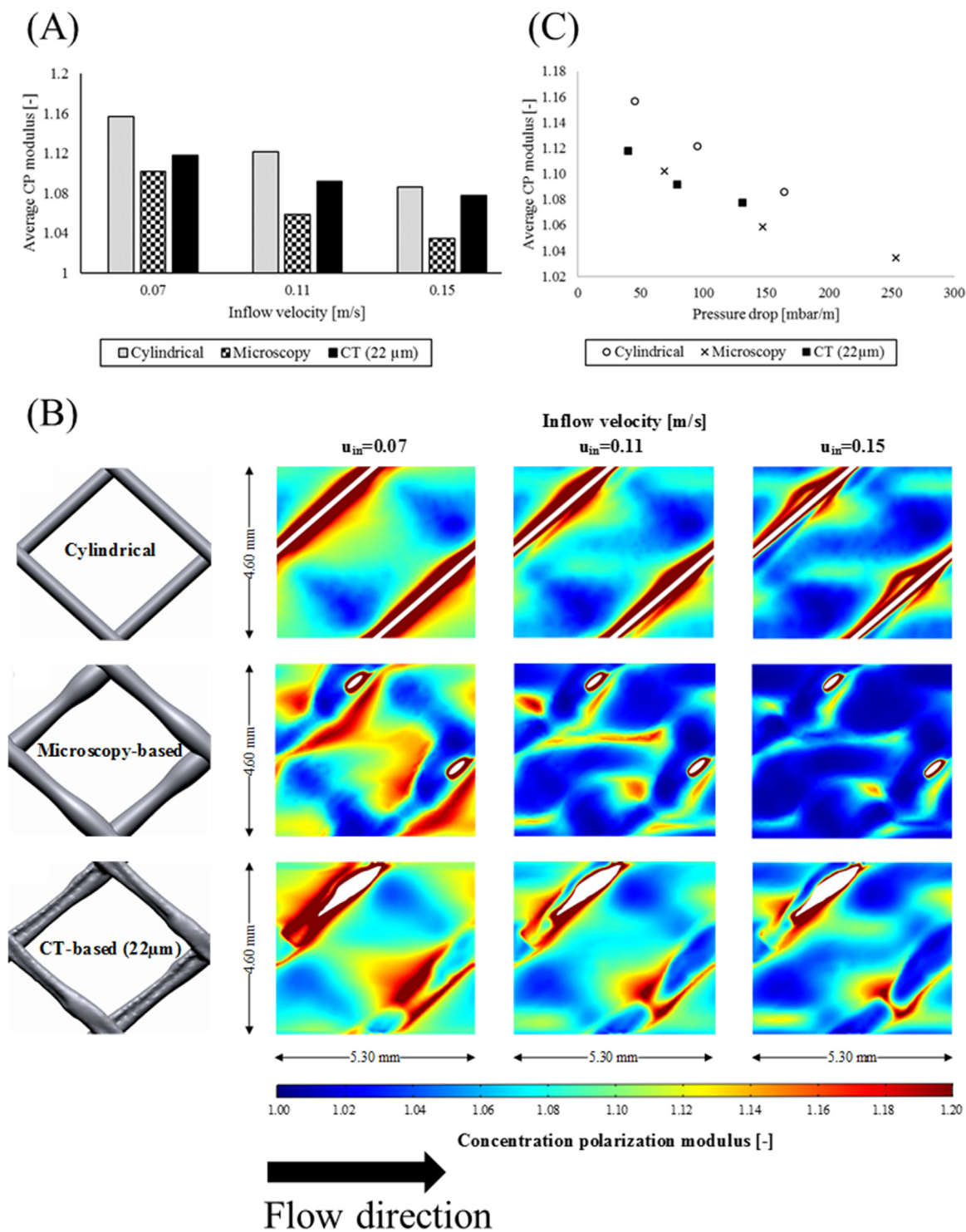
Fig. 8. (A) Average CP modulus at the bottom membrane for the different accuracy levels of spacer geometry representation. (B) Spatial distribution of concentration polarization modulus on the bottom membrane wall surface, for the three levels of spacer representation and for three inflow velocities (0.07, 0.11 and 0.15 m s^{-1}). For the ease of visual comparison, the color range was limited to a top value of CP 1.2. (C) Average CP modulus at the bottom membrane for the different accuracy levels of spacer geometry representation in dependency of the pressure drop.

different levels of spacer geometry accuracy and for three inflow velocities u_{in} (0.07, 0.11, 0.15 m s^{-1}) is displayed in Fig. 8A. Clearly, the average CP modulus in case of cylindrical spacer exceeds those for the microscopy- and CT-based spacers at all inflow velocities.

On the other hand, the microscopy-based spacer geometry consistently delivered the lowest values for the average CP. The reason for the elevated average CP modulus obtained in case of a cylindrical

spacer geometry representation is readily apparent from the solute concentration distribution over the membrane displayed in Fig. 8B. The cylindrical strands are completely attached to the membrane, resulting in regions of quasi-stagnant flow along the strands, which cause reduced salt transfer and larger solute concentrations. In the other geometry models, the strand thinning allows for improved depolarization by convective transport. On the extreme, the microscopy-based

geometry leaves the largest gaps between spacer strands and membrane, resulting in the least concentration polarization from all analyzed spacer geometries. The highest CT scan accuracy (5.5 μm) did not result in significantly different CP modulus results compared to the more imprecise CT scan accuracy (22 μm), as presented in the Supplementary material (Fig. S5).

With increasing pressure drop the CP modulus decreases for all spacer geometries (Fig. 8C). Overall, this study demonstrated the weakness of solute transport simulations if considering cylindrical spacer models. Neglecting the filament thinning leads to an over-prediction of average membrane solute concentrations compared to both the microscopy- and CT-based spacer geometries. In particular the more precise computation of the CP modulus at the filaments becomes important if the (bio)fouling formation and potential mitigation strategies are investigated. However, the reliability of solute transport simulations should be critically evaluated. The employed solute transport model was largely simplified and could only demonstrate the dependency of solute distribution at the membrane on the geometric quality of the spacer. Osmotic effects, concentration-dependence of viscosity and/or electrostatic interactions were not considered. The impact of solute concentration on solution viscosity and solute diffusion coefficient may not be considerable on the CP levels, as demonstrated by [24]. However, the omission of osmotic effects on permeation rate (e.g. the assumption of a constant permeation velocity) could be a more influential simplification. Nevertheless, the observed considerable differences in CP distribution between the largely different geometry models indicate that a sophisticated solute transport model is of little value without considering highly accurate spacer geometry, especially when quantitatively reliable concentration distributions are needed.

3.4. Particle deposition modeling and experimental tests

In order to evaluate potential effects of spacer geometry on the fouling patterns, particle transport and deposition simulations were performed for cylindrical, microscopy-based, and CT-based spacer geometries (Fig. 9A). The deposition pattern computed for the cylindrical geometry showed mainly large triangular areas formed by particles attached on the membrane surface. These appear upstream the entrance to the flow constriction created between a spacer strand and membrane, where the flow is directed towards to membrane. Furthermore, streaks appear along the main flow direction in the middle of a spacer element. The Microscopy- and CT-based models produce different deposition patterns from the cylindrical model. For lower cross-flow velocities (0.07 m s^{-1}) the deposition areas from the CT-based models are also triangular. Additional attachments upstream filament crossings appear in a "boomerang"-shape. For higher cross-flow velocities (> 0.11 m s^{-1}) the deposition patterns are only "boomerang"-shaped. On the other hand, the microscopy-based model produces only "boomerang"-shaped deposition zones at all velocities. With increasing cross-flow velocity the deposition pattern becomes more compact for all modeled geometries, while streaks start forming along the spacer element diagonal. Similar patterns were also identified by other modeling study [6] and observed experimentally in [31,32]. However, additional studies focusing on the qualitative and in particular on the quantitative comparison of numerical and experimental results will strengthen the assessment for practical membrane applications. Within this study abiotic particles were used for deposition pattern studies. Since these particles offer the advantage of controlled conditions (defined size, shape, and density, no growth) and are highly comparable with the numerical results, the effects of bacterial strains could behave differently. Our experimental tests of particle deposition performed for 0.07, 0.11 and 0.15 m s^{-1} (Fig. 9B) confirmed the model results. For 0.07 m s^{-1} the pronounced particle deposition membrane surface was recorded, with an area resembling the triangular deposition on the membrane. Very little particle deposition on the spacer filaments was noticed at the low velocity. In contrast, the experiments with 0.11 and 0.15 m s^{-1} show the presence of a "boomerang"-shape deposition area, together with more particles attached at the spacer filaments crossing. The experimental deposition patterns agree better with the microscopy-based model spacers and looser CT scan accuracies (all three CT scan accuracies particle modeling results are presented in the Supplementary material, Figure S6).

The developed approach could be useful in combination with the solute transport simulations as a (bio)fouling prediction tool (i.e.,
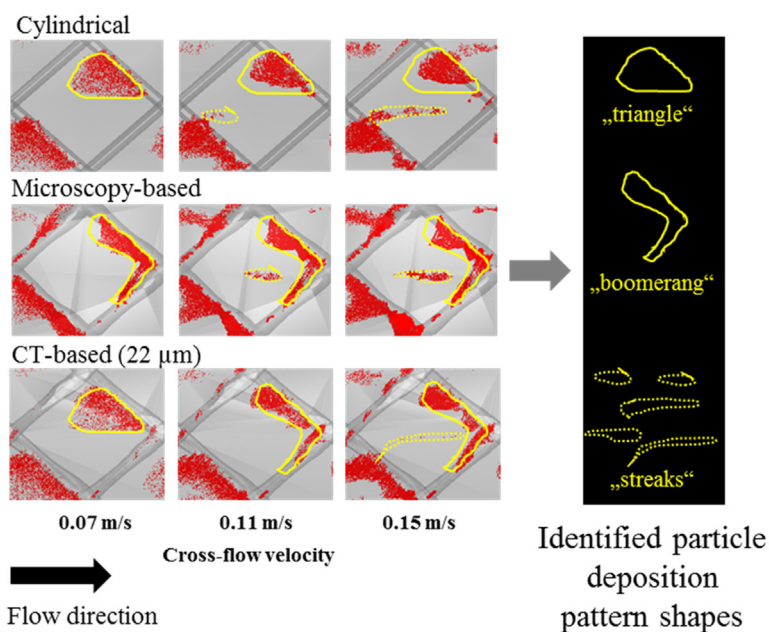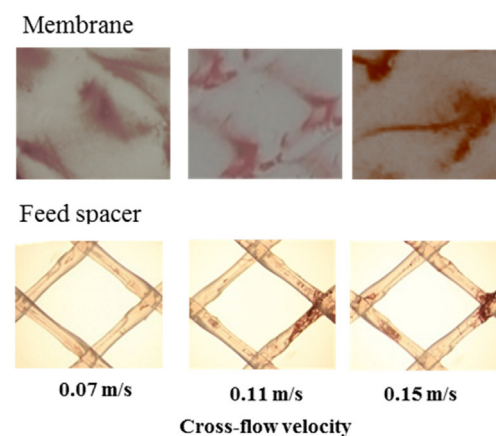

Fig. 9. (A) Computed particle deposition patterns of the bottom membrane wall with spacer geometries based on cylindrical filaments, top-view microscopy and CT scan (22 μm scan accuracy). (B) Experimental particle deposition tests at different flow velocities. Images show separately the deposition patterns on the flat-sheet membrane and feed spacer.

detecting areas on spacer and membrane more prone to fouling). In this context, Haidari et al. [33] measured low-velocity zones with particle image velocimetry (PIV), indicating high (bio)fouling potential in these areas. In a step forward, Siddiqui et al. [34] investigated the impact of geometric modifications of spacers as potential (bio)fouling mitigation.

4. Conclusions

The present work evaluated the impact of spacer model accuracy on numerical simulations of hydrodynamics and solute transport in feed channels of membrane processes. Based on three levels of geometric spacer model accuracy (cylindrical, microscopy-based, and X-ray computed tomography (CT)-based) and three CT scan accuracies, the conducted geometric evaluations, model solutions and experimental tests allowed the following conclusions:

- The CT scans yielded the most accurate spacer geometry model to date and revealed a more irregular, quasi-elliptic and not rotationally symmetric, shape of the filament cross-sections. Cylindrical and microscopy-based spacer models could not obtain this precise spacer geometry required for reliable simulations of hydrodynamics and solute transport.
- Thus, the spacer model accuracy affected significantly the hydrodynamics and solute transport simulations. Microscopic-based geometries failed to account the spacer ellipticity, resulting in overestimation of pressure drop by 80%, average velocity by more than 10% and average shear rate by $\sim$ 20% compared to CT-based geometries. Cylindrical spacer geometries neglected the spacer filament thinning, resulting in an overestimation of the concentration polarization at the membrane surface compared to CT-based geometries. However, the hydrodynamic simulations for cylindrical and CT-based spacers yielded relatively similar results for pressure drop, average velocity and average membrane shear rate. Please note that the agreement between cylindrical and CT-based spacer geometries regarding computed pressure drop, shear and velocity was only incidental, as the generated flow domain porosities were quite similar.
- The experimental measurements of pressure drop were in close agreement with simulations of pressure drop of the CT-based spacer geometries (highest deviation 14%)
- The particle deposition experimental test were in close agreement with the simulations of particle deposition of the CT-based spacer geometries. Experimentally-observed triangular areas at the membrane surface for the lower cross-flow velocity (0.07 m s^{-1}) and "boomerang"-shapes for higher cross-flow velocities ($>$ 0.11 m s^{-1}) were only reproduced by the CT-based simulations.
- Based on these results, we strongly recommend the use of the proposed CT scanning approach when quantitatively accurate CFD and solute transport simulations on cross-flow channels are targeted. However, an increased CT scan accuracy above a certain precision (i.e., less than 20 μm) in order to create more accurate spacer geometries did not result in significant changes in modeling results. The CT scan accuracy (within 5 and 20 μm) was found to have only marginal effects on the hydrodynamics and solute transport modeling results.

5. Outlook/recommendations for future studies

The assumption of laminar flow is justified for the range of investigated Reynolds numbers and it is not expected to introduce a major error. In a recent study, Bucs et al. [4] compared simulated laminar flow fields within spacer-obstructed cross-flow channels with PIV and found that for industry-typical flow velocities of 0.163 m s^{-1} Re = 160) the laminar flow model can deliver closely matching results [4]. Still, a PIV measurement should also be conducted for the investigated Toray spacer in order to confirm the source of observed differences in hydrodynamic patterns between the different spacer model accuracies.

Interestingly, almost all simulations conducted in [4] slightly overestimated the PIV observed velocities, which might stem from the potentially decreased flow domain porosity of the employed microscopy-based, rotationally symmetric spacer.

In this work only one commercial spacer was investigated. For this particular case of quasi-elliptic spacer strands, CT-based spacers constructed at all resolutions yielded similar results whereas both the cylindrical and the microscopy-based spacer models yielded strongly deviating results. For a spacer with more circular filaments, the observed differences between CT scanned and microscopically assessed spacer may not be so large. Therefore, the conclusions of this study may not be valid for all spacer types. Although Haaksman et al. [10] reported the same strong deviations between CT scanned and microscopy-based spacers for pressure drop for several, commercially available 34 mil spacers [10], more spacers should be evaluated in this regard in the future. In addition, different spacer types (e.g. woven spacers) should be analyzed.

The influence of the CT scan accuracy on the simulation results was investigated within an accuracy range of 5.5–20 μm. Within this range no significant influences of the CT scan on the simulations (hydrodynamics and solute transport) could be observed. With this knowledge it becomes evident that future studies could investigate the influence of courser CT scan accuracies (above 20 μm) and if there is a dependency of the detailed spacer geometry (e.g. comparison of very rough and very smooth spacer geometries).

Aside the investigated impact of spacer geometry accuracy on laminar flow and solute transport, the revealed quasi-elliptic shape of the filaments is expected to have also a considerable impact on the onset of unsteady and turbulent flow. Reported direct numerical simulations (DNS) on cross-flow channel hydrodynamics employed solely cylindrical filaments [16,35–37] or were conducted in 2-D domains [38–40]. In a next step, a DNS on the CT-based geometry will be conducted in order to evaluate the transient flow behavior and to determine the Reynolds numbers at which unsteady vortex shedding or full turbulence is reached. It is hypothesized that the quasi-elliptic, more streamlined shape of the filaments might delay the onset of unsteadiness and turbulence to higher Reynolds number than assumed to date [16]. On the other hand, the irregular, more complex shape could enhance the formation of unsteady vortices. DNS on a realistic geometry could confirm or challenge the hypothesis that spacers act as turbulence (mixing) promoters, with a far-ranging impact on future spacer design and optimization.

Finally, the presented procedure (i.e., CT scanning followed by surface fitting and generation of a periodic domain for fluid flow and solute transport simulations) could provide a useful workflow for membrane module developers to estimate reliably the performance of novel spacer geometries with optimized geometries. An optimal spacer geometry would be defined as a design that achieves a balance between competing factors, e.g., enhanced mass transfer vs. pressure drop and membrane fouling [5]. Combined with advances in 3-D-printing [41,42], the numerically optimized geometries can be readily tested and validated in experiments, as was presented in [43]. This validation by comparison of numerical and experimental tests would strengthen the practical impact of spacer geometry development. On the other hand, provided sufficient accuracy, in situ CT scanning could reveal non-intentional behavior of spacer placed in real modules, e.g., deformations, curvature effects, or even scaling patterns. Since simulations did not considering the curvature of spiral-wound membrane modules, future studies could investigate the deviation of flat and curvature geometries. However, in 2-D simulations of the pressure drop the influence of curvature was found to be less than 1% compared to flat geometries [44].

Overall, the development of optimized spacer geometries resulting in optimized hydraulic conditions of the feed channel has potential to lower the energy requirements of membrane treatment and reducing (bio)fouling phenomena [5,34,42].

Acknowledgements

Appendix A. Supporting information

Supplementary data associated with this article can be found in the online version at doi:10.1016/j.memsci.2018.07.006.

References

[1] T. Melin, R. Rautenbach, Membranverfahren, third ed., Springer-Verlag, Berlin Heidelberg, 2007, https://doi.org/10.1007/978-3-540-34328-8.

[2] J.S. Vrouwenvelder, C. Picioreanu, J.C. Kruithof, M.C.M. van Loosdrecht, Biofouling in spiral wound membrane systems: three-dimensional CFD model based evaluation of experimental data, J. Membr. Sci. 346 (2010) 71–85, https://doi.org/10.1016/j.memsci.2009.09.025.

[3] J. Johnson, M. Busch, Engineering aspects of reverse osmosis module design, Desalin. Water Treat. 15 (2010) 236–248, https://doi.org/10.5004/dwt.2010.1756.

[4] Sz.S. Bucs, R. Valladares Linares, J.O. Marston, A.I. Radu, J.S. Vrouwenvelder, C. Picioreanu, Experimental and numerical characterization of the water flow in spacer-filled channels of spiral-wound membranes, Water Res. 87 (2015) 299–310, https://doi.org/10.1016/j.watres.2015.09.036.

[5] A.H. Haidari, S.G.J. Heijman, W.G.J. van der Meer, Optimal design of spacers in reverse osmosis, Sep. Purif. Technol. 192 (2018) 441–456, https://doi.org/10.1016/j.seppur.2017.10.042.

[6] A.I. Radu, M.S.H. van Steen, J.S. Vrouwenvelder, M.C.M. van Loosdrecht, C. Picioreanu, Spacer geometry and particle deposition in spiral wound membrane feed channels, Water Res. 64 (2014) 160–176, https://doi.org/10.1016/j.watres.2014.06.040.

[7] C. Picioreanu, J.S. Vrouwenvelder, M.C.M. van Loosdrecht, Three-dimensional modeling of biofouling and fluid dynamics in feed spacer channels of membrane devices, J. Membr. Sci. 345 (2009) 340–354, https://doi.org/10.1016/j.memsci.2009.09.024.

[8] M. Shakaib, S.M.F. Hasani, M. Mahmood, Study on the effects of spacer geometry in membrane feed channels using three-dimensional computational flow modeling, J. Membr. Sci. 297 (2007) 74–89, https://doi.org/10.1016/j.memsci.2007.03.010.

[9] A. Saeed, R. Vuthaluru, Y. Yang, H.B. Vuthaluru, Effect of feed spacer arrangement on flow dynamics through spacer filled membranes, Desalination 285 (2012) 163–169, https://doi.org/10.1016/j.desal.2011.09.050.

[10] V.A. Haaksman, A. Siddiqui, C. Schellenberg, J. Kidwell, J.S. Vrouwenvelder, C. Picioreanu, Characterization of feed channel spacer performance using geometries obtained by X-ray computed tomography, J. Membr. Sci. 522 (2017) 124–139, https://doi.org/10.1016/j.memsci.2016.09.005.

[11] B. Gu, C.S. Adjiman, X.Y. Xu, The effect of feed spacer geometry on membrane performance and concentration polarisation based on 3D CFD simulations, J. Membr. Sci. 527 (2017) 78–91, https://doi.org/10.1016/j.memsci.2016.12.058.

[12] O. Kavianipour, G.D. Ingram, H.B. Vuthaluru, Investigation into the effectiveness of feed spacer configuraions for reverse osmosis membrane modules using Computational Fluid Dynamics, J. Membr. Sci. 526 (2017) 156–171, https://doi.org/10.1016/j.memsci.2016.12.034.

[13] A. Siddiqui, S. Lehmann, V. Haaksman, J. Ogier, C. Schellenberg, M.C.M. van Loosdrecht, J.C. Kruithof, J.S. Vrouwenvelder, Porosity of spacer-filled channels in spiral-wound membrane systems: quantification methods and impact on hydraulic characterization, Water Res. 119 (2017) 304–311, https://doi.org/10.1016/j.watres.2017.04.034.

[14] Sz.S. Bucs, A.I. Radu, V. Lavric, J.S. Vrouwenvelder, C. Picioreanu, Effect of different commercial feed spacers on biofouling of reverse osmosis membrane systems: a numerical study, Desalination 343 (2014) 26–37, https://doi.org/10.1016/j.desal.2013.11.007.

[15] Y.L. Li, K.L. Tung, CFD simulation of fluid flow through spacer-filled membrane module: selecting suitable cell types for periodic boundary conditions, Desalination 233 (2008) 351–358, https://doi.org/10.1016/j.desal.2007.09.061.

[16] S.M. Mojab, A. Pollard, J.G. Pharoah, S.B. Beale, E.S. Hanff, Unsteady laminar to turbulent flow in a spacer-filled channel, Flow Turbul. Combust. 92 (2014) 563–577, https://doi.org/10.1007/s10494-013-9514-4.

[17] S. Al-Sharif, M. Albeirutty, A. Cipollina, G. Micale, Modelling flow and heat transfer in spacer-filled membrane distillation channels using open source CFD code, Desalination 311 (2013) 103–112, https://doi.org/10.1016/j.desal.2012.11.005.

[18] K.K. Lau, M.Z. Abu Bakar, A.L. Ahmad, T. Murugesan, Feed spacer mesh angle: 3D modeling, simulation and optimization based on unsteady hydrodynamic in spiral wound membrane channel, J. Membr. Sci. 343 (2009) 16–33, https://doi.org/10.1016/j.memsci.2009.07.001.

[19] S. Karode, A. Kumar, Flow visualization through spacer filled channels by computational fluid dynamics I. Pressure drop and shear rate calculations for flat sheet geometry, J. Membr. Sci. 193 (2001) 69–84, https://doi.org/10.1016/S0376-7388(01)00494-X.

[20] G. Schock, A. Miquel, Mass transfer and pressure loss in spiral wound modules, Desalination 64 (1987) 339–352, https://doi.org/10.1016/0011-9164(87)90107-X.

[21] G.A. Fimbres-Weihs, D.E. Wiley, Review of 3D CFD modeling of flow and mass transfer in narrow spacer-filled channels in membrane modules, Chem. Eng. Process. Process. Intensif 49 (2010) 759–781, https://doi.org/10.1016/j.cep.2010.01.007.

[22] A.J. Karabelas, M. Kostoglou, C.P. Koutsou, Modeling of spiral wound membrane desalination modules and plants – review and research priorities, Desalination 356 (2015) 165–186, https://doi.org/10.1016/j.desal.2014.10.002.

[23] A.R. Rajabzadeh, Membrane Fouling During Hollow Fiber Ultrafiltration of Protein Solutions: Computational Fluid Modeling and Physicochemical Properties (Doctoral Thesis), University of Waterloo, Canada, 2010〈http://hdl.handle.net/10012/5786〉.

[24] E. Lyster, J. Au, R. Rallo, F. Giralt, Y. Cohen, Coupled 3-D hydrodynamics and mass transfer analysis of mineral scaling-induced flux decline in a laboratory plate-and-frame reverse osmosis membrane module, J. Membr. Sci. 339 (2009) 39–48, https://doi.org/10.1016/j.memsci.2009.04.024.

[25] J.S. Vrouwenvelder, J.A.M. van Paassen, L.P. Wessels, A.F. van Dam, S.M. Bakker, The membrane fouling simulator: a practical tool for fouling prediction and control, J. Membr. Sci. 281 (2006) 316–324, https://doi.org/10.1016/j.memsci.2006.03.046.

[26] J.S. Vrouwenvelder, J.A.M. van Paassen, J.C. Kruithof, M.C.M. van Loosdrecht, Sensitive pressure drop measurement of individual lead membrane elements for accurate early biofouling detection, J. Membr. Sci. 338 (2009) 92–99, https://doi.org/10.1016/j.memsci.2009.04.016.

[27] Sz.S. Bucs, N. Farhat, A. Siddiqui, R.V. Linares, A. Radu, J.C. Kruithof, J.S. Vrouwenvelder, Development of a setup to enable stable and accurate flow conditions for membrane biofouling studies, Desalin. Water Treat. 57 (2016) 12893–12901, https://doi.org/10.1080/19443994.2015.1057037.

[28] P. Pánek, R. Kodým, D. Šnita, K. Bouzek, Spatially two-dimensional mathematical model of the flow hydrodynamics in a spacer-filled channel – the effect of inertial forces, J. Membr. Sci. 492 (2015) 588–599, https://doi.org/10.1016/j.memsci.2015.03.099.

[29] J.L.C. Santos, V. Geraldes, S. Velizarov, J.G. Crespo, Investigation of flow patterns and mass transfer in membrane module channels filled with flow-aligned spacers using computational fluid dynamics (CFD), J. Membr. Sci. 305 (2007) 103–117, https://doi.org/10.1016/j.memsci.2007.07.036.

[30] M. Shakaib, S.M.F. Hasani, M. Mahmood, Study on the effects of spacer geometry in membrane feed channels using three-dimensional computational flow modeling, J. Membr. Sci. 297 (2007) 74–89, https://doi.org/10.1016/j.memsci.2007.03.010.

[31] L. Fortunato, T. Leiknes, In-situ biofouling assessment in spacer filled channels using optical coherence tomography (OCT): 3D biofilm thickness mapping, Bioresour. Technol. 229 (2017) 231–235, https://doi.org/10.1016/j.biortech.2017.01.021.

[32] S. West, M. Wagner, C. Engelke, H. Horn, Optical coherence tomography for the in situ three-dimensional visualization and quantification of feed spacer channel fouling in reverse osmosis membrane modules, J. Membr. Sci. 498 (2016) 345–352, https://doi.org/10.1016/j.memsci.2015.09.047.

[33] A.H. Haidari, S.G.J. Heijman, W.G.J. van der Meer, Visualization of hydraulic conditions inside the feed channel of reverse osmosis: a practical comparison of velocity between empty and spacer-filled channel, Water Res. 106 (2016) 232–241, https://doi.org/10.1016/j.watres.2016.10.012.

[34] A. Siddiqui, S. Lehmann, Sz.S. Bucs, M. Fresquet, L. Fel, E.I.E.C. Prest, J. Ogier, C. Schellenberg, M.C.M. van Loosdrecht, J.C. Kruithof, J.S. Vrouwenvelder, Predicting the impact of feed spacer modification on biofouling by hydraulic characterization and biofouling studies in membrane fouling simulators, Water Res. 110 (2017) 281–287, https://doi.org/10.1016/j.watres.2016.12.034.

[35] C.P. Koutsou, S.G. Yiantsios, J. Karabelas, A numerical and experimental study of mass transfer in spacer-filled channels: effects of spacer geometrical characteristics and Schmidt number, J. Membr. Sci. 326 (2009) 234–251, https://doi.org/10.1016/j.memsci.2008.10.007.

[36] C.P. Koutsou, S.G. Yiantsios, A.J. Karabelas, Direct numerical simulation of flow in spacer-filled channels: effect of spacer geometrical characteristics, J. Membr. Sci. 291 (2007) 53–69, https://doi.org/10.1016/j.memsci.2006.12.032.

[37] F. Li, W. Meindersma, B. De Haan, T. Reith, Optimization of commercial net spacers in spiral wound membrane modules, J. Membr. Sci. 208 (2002) 289–302, https://doi.org/10.1016/S0376-7388(02)00307-1.

[38] M. Amokrane, D. Sadaoui, C.P. Koutsou, A.J. Karabelas, M. Dudeck, A study of flow field and concentration polarization evolution in membrane channels with two-dimensional spacers during water desalination, J. Membr. Sci. 477 (2015) 139–150, https://doi.org/10.1016/j.memsci.2014.11.029.

[39] A.L. Ahmad, K.K. Lau, Impact of different spacer filaments geometries on 2D unsteady hydrodynamics and concentration polarization in spiral wound membrane channel, J. Membr. Sci. 286 (2006) 77–92, https://doi.org/10.1016/j.memsci.2006.09.018.

[40] C.P. Koutsou, S.G. Yiantsios, A.J. Karabelas, Numerical simulation of the flow in a plane-channel containing a periodic array of cylindrical turbulence promoters, J. Membr. Sci. 231 (2004) 81–90, https://doi.org/10.1016/j.memsci.2003.11.005.

[41] J.Y. Lee, W.S. Tan, J. An, C.K. Chua, C.Y. Tang, A.G. Fane, T.H. Chong, The potential to enhance membrane module design with 3D printing technology, J. Membr. Sci. 499 (2016) 480–490, https://doi.org/10.1016/j.memsci.2015.11.008.

[42] Sz.S. Bucs, N. Farhat, J.C. Kruithof, C. Picioreanu, M.C.M. van Loosdrecht, J.S. Vrouwenvelder, Review on strategies for biofouling mitigation in spiral wound membrane systems, Desalination (2018), https://doi.org/10.1016/j.desal.2018.01.023 (In press).

[43] A. Siddiqui, N. Farhat, Sz.S. Bucs, R. Valladares, C. Picioreanu, J.C. Kruithof, Development and characterization of 3D-printed feed spacers for spiral wound membrane systems, Water Res. 91 (2016) 55–67, https://doi.org/10.1016/j.watres.2015.12.052.

[44] Y.-L. Li, K.-L. Tung, The effect of curvature of a spacer-filled channel on fluid flow in spiral-wound membrane modules, J. Membr. Sci. 319 (2008) 286–297, https://doi.org/10.1016/j.memsci.2008.03.069.